Article:
Bin-Mohsin, B and Lesnic, D orcid.org/0000-0003-3025-2770 (2019) Reconstruction of a volumetric source domain. Journal of Computational Methods in Sciences and Engineering, 19 (2). pp. 367-385. ISSN 1472-7978

https://doi.org/10.3233/JCM-180878

Reconstruction of a volumetric source domain

B. Bin-Mohsin[1] and D. Lesnic[2]

[1]*Department of Mathematics, College of Science, King Saud University, PO. Box 2455 Riyadh 11451, Saudi Arabia*
[2]*Department of Applied Mathematics, University of Leeds, Leeds LS2 9JT, UK*
balmohsen@ksu.edu.sa (B. Bin-Mohsin), amt5ld@maths.leeds.ac.uk (D. Lesnic)

Abstract

Inverse and ill-posed problems which consist of reconstructing the unknown support of a three-dimensional volumetric source from a single pair of exterior boundary Cauchy data are investigated. The underlying dependent variable may satisfy the Laplace, Poisson, Helmholtz or modified Helmholtz equations. In the case of a constant physical properties the solutions of these elliptic PDEs are sought as linear combinations of fundamental solutions, as in the method of fundamental solutions (MFS). The unknown source domain is parametrized by the radial coordinate, as a function of the spherical angles. The resulting least-squares functional estimating the gap between the measured and the computed data is regularized and minimized using the `lsqnonlin` toolbox routine in Matlab. Numerical results are presented and discussed for both exact and noisy data, confirming the accuracy and stability of reconstruction.

Keywords: Inverse problem; Method of fundamental solutions; Nonlinear optimization; Source domain identification.

1 Introduction

Determination of the location, size and shape of an anomaly/defect present inside a given specimen from non-destructive boundary measurements represents one of the most difficult inverse problems because it is both ill-posed and nonlinear. The nonlinearity arises due to the unknown geometry of the solution domain, whilst the ill-posedness arises due to the non-uniqueness of identification or the unstable features of an unregularized reconstruction.

In this paper, the determination of the support of a volumetric source from non-destructive knowledge of the Cauchy boundary data is investigated. This formulation is closely related to the inverse gravimetry problem concerning the determination of the density of the interior of the Earth from gravimetric surface measurements, [11].

Prior to the present numerical study, the reconstruction of a source domain from boundary measurements has been investigated mainly theoretically in cases where the underlying

medium was subject to various excitations such as electrical, i.e. Laplace's/Poisson's equation for the potential in electroencephalography, [4, 14], thermal, i.e. the modified Helmholtz equation for the temperature in a fin, [20], or acoustics, i.e. the Helmholtz equation for the pressure, [10].

In this paper, the aim is to reconstruct numerically in a stable and accurate manner the volumetric source domain of constant physical properties by employing a combined meshless technique with nonlinear optimization, which recently has been developed by the authors, [3], in the two-dimensional planar case. This nontrivial three-dimensional extension and its computational implementation, and numerical results represent the main novelty of the current study.

The plan of the paper is as follows. In Section 2, we introduce the mathematical formulation of the inverse source domain problem and state the available uniqueness results. In Section 3, we describe the method of fundamental solutions (MFS) with the inhomogeneity removal, as well as the nonlinear minimization proposed for reconstructing the star-shape support of the unknown source. Section 4 presents and discusses thoroughly numerical results in which the convergence of the objective function with the number of iterations is analysed. Also, the stability of the numerical solution with respect to noise in the input data is investigated. Finally, Section 5 presents the conclusions of the work.

2 Mathematical formulation

Let us consider the practical application of recovering an unknown mass distribution inside a three-dimensional body from measurements of the potential and flux on the boundary, [21]. Suppose the mass distribution consists of two layers Ω_1 and Ω_2 covering the body Ω (the Earth), a region of constant (unit) density inside Ω_2 (a core) and an annular region $\Omega_1 = \Omega \backslash \Omega_2$ (a mantle) enclosing the core. In physical terms, the gravitational potential u generated by this mass distribution is then given by equation

$$\nabla^2 u + \kappa^2 u = \chi_{\Omega_2} \quad \text{in } \Omega, \tag{1}$$

where χ_{Ω_2} denotes the characteristic function of the domain Ω_2, (equal to 1 in Ω_2 and 0 in Ω_1) and κ is a known real or complex number or function characterising the physical properties of the medium Ω. Then the inverse problem consists of determining the support $\Omega_2 \subset \Omega \subset \mathbb{R}^3$ of an unknown volumetric source of unit strength/intensity, in the elliptic equation (1) from non-destructive Cauchy data measurements

$$u = f \quad \text{and} \quad \frac{\partial u}{\partial n} = g \quad \text{on} \quad \partial\Omega, \tag{2}$$

where n denotes the outward unit normal to the boundary $\partial\Omega$. In (2), the Cauchy data satisfy $0 \not\equiv f \in H^{1/2}(\partial\Omega)$ and $g \in H^{-1/2}(\partial\Omega)$ such that u belongs to $H^1(\Omega)$.

Partial Cauchy data of the form

$$u = f \quad \text{on} \quad \partial\Omega \quad \text{and} \quad \frac{\partial u}{\partial n} = g \quad \text{on} \quad \Gamma \subset \partial\Omega, \tag{3}$$

where Γ is a subset of $\partial\Omega$ of positive measure, can also be investigated. The assumption of a unit strength source in the right-hand side of (1) is not a restriction and it can be a function

$h(x)\chi_{\Omega_2}$ for $x \in \Omega$. In this case, one can approximate the inhomogeneity $h(x)$ by a linear combination of globally defined radial basis functions, as in the dual reciprocity method, and combine with the MFS, as described in [8].

Let us also mention that another formulation of the above problem can be viewed in the steady-state thermal imaging context to recover the shape and location of a heat source of known intensity. This then would have practical application in the detection of tumours, since cancerous cells have higher metabolic rates leading to regions of higher heat source generation than the surrounding healthy tissue, [9].

We assume that the domains Ω and Ω_2 are bounded and that $\Omega_1 := \Omega \backslash \Omega_2$ is connected. Futher, we assume the boundaries $\partial\Omega$ and $\partial\Omega_2$ being smooth though Lipschitz boundaries can also be considered. By defining

$$u := \begin{cases} u_1 & \text{in } \Omega_1, \\ u_2 & \text{in } \Omega_2, \end{cases} \tag{4}$$

equations (1) and (4) give rise to the following transmission problem:

$$\nabla^2 u_1 + \kappa^2 u_1 = 0 \quad \text{in } \Omega_1, \tag{5}$$

$$\nabla^2 u_2 + \kappa^2 u_2 = 1 \quad \text{in } \Omega_2, \tag{6}$$

$$u_1 = u_2 \quad \text{on } \partial\Omega_2, \tag{7}$$

$$\frac{\partial u_1}{\partial n} = \frac{\partial u_2}{\partial n} \quad \text{on } \partial\Omega_2, \tag{8}$$

$$u_1 = f \quad \text{on } \partial\Omega, \tag{9}$$

$$\frac{\partial u_1}{\partial n} = g \quad \text{on } \partial\Omega, \tag{10}$$

in which the interfacial boundary $\partial\Omega_2$ separating the core from the mantle is unknown and has to be reconstructed.

In the case of Poisson's equation, i.e. $\kappa = 0$ in (1), we have uniqueness of Ω_2 in the class of star-shaped domains, [9, 11-13]. In the case of the modified Helmholtz equation, i.e. $\kappa = i\kappa'$, where i is the imaginary unit, with $\kappa' \in \mathbb{R}_+^*$ in (1), we have uniqueness of Ω_2 in the class of convex domains provided that, in addition, u is prescribed in an interior a priori known ball included in Ω_2, [11, 20]. Finally, in the case of the Helmholtz equation, i.e. $\kappa \in \mathbb{R}_+^*$ in (1), indications have been given in [10] that if Ω_2 is a polyhedron, then one can recover uniquely the convex hull $[\Omega_2]$ of Ω_2 in the problem (5)-(10).

The next task is to reconstruct the source domain Ω_2 numerically. Recently, the MFS has proved, [2, 3, 19], easy to use in detecting cavities, rigid inclusions, as well as inhomogeneities in inverse geometric problems governed by the modified Helmholtz equation. For a recent review of the MFS, as applied to solving inverse geometric problems, [17]. In this paper, we investigate yet another application of the MFS to reconstruct the source volumetric domain Ω_2 from the Cauchy data (9) and (10).

3 The method of fundamental solutions (MFS)

For the application of the MFS we require κ to be constant. First, we need to move the right-hand side unit inhomogeneity in (6) to the boundary conditions (7)-(10). For this, we decompose

$$u_2 = u_2^h + u_2^p, \tag{11}$$

where the homogeneous part u_2^h satisfies

$$\nabla^2 u_2^h + \kappa^2 u_2^h = 0 \quad \text{in } \Omega_2, \tag{12}$$

and the inhomogeneous part is just a particular solution of equation (6) (in the whole $\mathbb{R}^3$) given by, see e.g. [15],

$$u_2^p(x) = \frac{|x|^2}{6}, \quad \text{if } \kappa = 0, \tag{13}$$

$$u_2^p(x) = \frac{1}{\kappa^2} + \begin{cases} \frac{\sinh(-i\kappa|x|)}{|x|} & \text{if } i\kappa \in \mathbb{R}_-^* \\ \frac{\sin(\kappa|x|)}{|x|} & \text{if } \kappa \in \mathbb{R}_+^* \end{cases} \tag{14}$$

where the limits in (14) are equal to $-i\kappa$, if $i\kappa \in \mathbb{R}_-^*$, and κ, if $\kappa \in \mathbb{R}_+^*$ at the origin $x = 0$.

With the superposition (11), the transmission interface conditions (7) and (8) become

$$u_1 = u_2^h + u_2^p \quad \text{on } \partial\Omega_2, \tag{15}$$

$$\frac{\partial u_1}{\partial n} = \frac{\partial u_2^h}{\partial n} + \frac{\partial u_2^p}{\partial n} \quad \text{on } \partial\Omega_2. \tag{16}$$

On applying the MFS we approximate the solutions u_1 and u_2^h of the elliptic homogeneous equations (5) and (6) by finite linear combinations of fundamental solutions of the form

$$u_{1,2NM}(x) = \sum_{S=1}^{2} \sum_{i=1}^{N} \sum_{j=1}^{M} a_{i,j}^S G_\kappa(x, \xi_S^{i,j}), \quad x \in \overline{\Omega}_1, \tag{17}$$

$$u_{2,NM}^h(x) = \sum_{i=1}^{N} \sum_{j=1}^{M} b_{i,j} G_\kappa(x, \xi_3^{i,j}), \quad x \in \overline{\Omega}_2, \tag{18}$$

where $\mathbf{a} = (a_{i,j}^S)_{i=\overline{1,N}, j=\overline{1,M}, S=1,2}$ and $\mathbf{b} = (b_{i,j})_{i=\overline{1,N}, j=\overline{1,M}}$ are unknown coefficients to be determined, $(\xi_S^{i,j})_{i=\overline{1,N}, j=\overline{1,M}, S=1,2}$ are source points located outside the annular domain $\overline{\Omega}_1$, $(\xi_3^{i,j})_{i=\overline{1,N}, j=\overline{1,M}}$ are source points located outside the domain $\overline{\Omega}_2$, and G_κ is the fundamental solution of the three-dimensional elliptic equation $\nabla^2 u + \kappa^2 u = 0$ given by, see e.g. [1],

$$G_\kappa(x, \xi) = \begin{cases} \frac{1}{|x-\xi|} & \text{if } \kappa = 0 \\ \frac{\exp(-i\kappa|x-\xi|)}{|x-\xi|} & \text{if } i\kappa \in \mathbb{R}_-^* \\ \frac{\exp(i\kappa|x-\xi|)}{|x-\xi|} & \text{if } \kappa \in \mathbb{R}_+^* \end{cases} \tag{19}$$

We remark that the normalisation constants usually appearing in the fundamental solution (19) have been omitted, as they were incorporated in the unknown coefficients $\mathbf{a}$ and $\mathbf{b}$ in (17) and (18), respectively. In the case of the Helmholtz equation when $\kappa \in \mathbb{R}_+^*$ we can avoid using the complex version of the fundamental solution in (19) by considering instead only the non-singular part

$$G_\kappa(x,\xi) = \frac{\sin(\kappa|x-\xi|)}{|x-\xi|} \qquad \text{if} \quad \kappa \in \mathbb{R}_+^*, \tag{20}$$

as in the boundary knot method, [1, 5]. Finally, we mention that all the analysis of the section can easily be extended to include anisotropic homogeneous materials having as their leading part in (1) the anisotropic Laplace-Beltrami operator $\sum_{i,j=1}^3 K_{ij}\frac{\partial^2 u}{\partial x_i \partial x_j}$, where $(K_{ij})_{i,j=\overline{1,3}}$ denotes the symmetric and positive conductivity tensor. The main change then is to replace the radial distance $|x|$ by the geodesic distance $x^T K^{-1} x$, see e.g. [16].

In comparison with domain discretisation methods such as the finite element or the finite-difference method, the MFS possesses the same advantages and disadvantages as the boundary element method (BEM) has, namely, no discretization of the domain is needed, however it relies on the fundamental solution of the governing operator being available explicitly. Furthermore, in comparison with the BEM, by placing the source points on an exterior pseudo-boundary, the MFS avoids the evaluation of singular integrals, however the drawback is that the location of these source points introduces an additional dilation/contraction parameter whose choice has to be optimized. Moreover, the BEM discretization of the boundary, which may become complicated especially for three-dimensional irregular shapes, is not needed in the MFS which can place the sources simply on a sphere surrounding the solution domain.

In what follows, we explain the inverse methodology in three-dimensions, see also [18] for a related problem MFS implementation.

The source points $(\xi_1^{i,j})_{i=\overline{1,N},j=\overline{1,M}} \notin \overline{\Omega}$ are placed on a (fixed) dilated pseudo-boundary $\partial\Omega'$ of similar shape as $\partial\Omega$. The remaining source points $(\xi_2^{i,j})_{i=\overline{1,N},j=\overline{1,M}} \in \Omega_2$ and $(\xi_3^{i,j})_{i=\overline{1,N},j=\overline{1,M}} \notin \overline{\Omega}_2$ are placed on contraction and dilation (moving) pseudo-boundaries $\partial\Omega_2'$ and $\partial\Omega_2''$ similar to $\partial\Omega_2$ at a distance $\delta > 0$ in the inward and outward directions, respectively.

Without loss of generality, we may assume that the domain Ω is a unit ball $B(\mathbf{0};1)$. We also assume that the unknown support Ω_2 is star-shaped with respect to the origin, i.e.

$$\partial\Omega_2 = \Big\{ r(\theta,\phi)\big(\cos(\theta)\sin(\phi), \sin(\theta)\sin(\phi), \cos(\phi)\big) |\ \theta \in [0,2\pi), \phi \in [0,\pi) \Big\}, \tag{21}$$

where r is a smooth function with values in $(0,1)$. With this star-shaped assumption, the uniqueness of the support Ω_2 holds, at least in the case $\kappa = 0$, [9, 11-13], as already mentioned in Section 2. In this setup of particular domains Ω and Ω_2, the boundary collocation and source points are uniformly distributed, as follows:

$$\begin{aligned} X_{i,j}^1 &= (\cos(\theta_i)\sin(\phi_j), \sin(\theta_i)\sin(\phi_j), \cos(\phi_j)), \\ X_{i,j}^2 &= r(\theta_i,\phi_j)\Big(\cos(\theta_i)\sin(\phi_j), \sin(\theta_i)\sin(\phi_j), \cos(\phi_j)\Big),\ i = \overline{1,N}, j = \overline{1,M}, \end{aligned} \tag{22}$$

$$\begin{aligned} \xi_1^{k,\ell} &= R\Big(\cos(\tilde{\theta}_k)\sin(\tilde{\phi}_\ell), \sin(\tilde{\theta}_k)\sin(\tilde{\phi}_\ell), \cos(\tilde{\phi}_\ell)\Big), \quad \xi_2^{k,\ell} = (1-\delta)X_{k,\ell}^2, \\ \xi_3^{k,\ell} &= (1+\delta)X_{k,\ell}^2, \quad k = \overline{1,N}, \ell = \overline{1,M}, \end{aligned} \tag{23}$$

where

$$\theta_i = 2\pi i/N, \quad i = \overline{1,N}, \quad \phi_j = \pi j/M, \quad j = \overline{1,M},$$
$$\tilde{\theta}_k = 2\pi k/N, \quad k = \overline{1,N}, \quad \tilde{\phi}_\ell = \pi \ell/M, \quad \ell = \overline{1,M},$$

$r_{i,j} := r(\theta_i, \phi_j)$ for $i = \overline{1,N},\ j = \overline{1,M}$, $R > 1$ and $\delta \in (0,1)$.

The unknown radii $\mathbf{r} = (r_{i,j})_{i=\overline{1,N}, j=\overline{1,M}}$, characterising the star-shaped support Ω_2, together with the unknown MFS coefficients $\mathbf{a}$ and $\mathbf{b}$, giving the approximations of the solutions u_1 and u_2, are simultaneously determined by imposing the transmission conditions (15), (16) and the Cauchy data (9), (10) at the collocating points (22) in a least-squares sense. This results into minimizing the following (regularized) least-squares nonlinear objective function:

$$T(\mathbf{a},\mathbf{b},\mathbf{r}) := \left\| u_1 - f \right\|^2_{L^2(\partial\Omega)} + \left\| \frac{\partial u_1}{\partial n} - g^\epsilon \right\|^2_{L^2(\partial\Omega)} + \left\| u_1 - u_2^h - u_2^p \right\|^2_{L^2(\partial\Omega_2)}$$
$$+ \left\| \frac{\partial u_1}{\partial n} - \frac{\partial u_2^h}{\partial n} - \frac{\partial u_2^p}{\partial n} \right\|^2_{L^2(\partial\Omega_2)} + \lambda_1 \left\{ \|\mathbf{a}\|^2 + \|\mathbf{b}\|^2 \right\} + \lambda_2 \{ \|\mathbf{r}_\theta\|^2 + \|\mathbf{r}_\phi\|^2 \}, \tag{24}$$

where $\lambda_1,\ \lambda_2 \geq 0$ are regularization parameters to be prescribed. These parameters are introduced in order to ensure/improve the stability of the nonlinear Tikhonov regularization functional (24). In (24), the Neumann data (10) was input as being a noisy perturbation g^ϵ of the exact data g in order to simulate the errors which are inherently present in any practical measurement. Finally, the last term in (24) represents a first-order derivative smoothness constraint on our desired shape for Ω_2, and is defined as:

$$\|\mathbf{r}_\theta\|^2 = \sum_{i=2}^{N} \sum_{j=1}^{M} \left(\frac{r_{i,j} - r_{i-1,j}}{2\pi/N} \right)^2, \quad \|\mathbf{r}_\phi\|^2 = \sum_{i=1}^{N} \sum_{j=2}^{M} \left(\frac{r_{i,j} - r_{i,j-1}}{\pi/M} \right)^2. \tag{25}$$

Introducing the MFS approximations (17) and (18) into (24) results in

$$
\begin{aligned}
T(\mathbf{a},\mathbf{b},\mathbf{r}) = &\sum_{i=1}^{N}\sum_{j=1}^{M}\left[\sum_{S=1}^{2}\sum_{k=1}^{N}\sum_{\ell=1}^{M} a_{k,\ell}^{S} G_\kappa(X_{i,j}^1,\xi_S^{k,\ell}) - f(X_{i,j}^1)\right]^2 \\
&+\sum_{i=N+1}^{2N}\sum_{j=M+1}^{2M}\left[\sum_{S=1}^{2}\sum_{k=1}^{N}\sum_{\ell=1}^{M} a_{k,\ell}^{S} \frac{\partial G_\kappa}{\partial n}(X_{i-N,j-M}^1,\xi_S^{k,\ell}) - g^\epsilon(X_{i-N,j-M}^1)\right]^2 \\
&+\sum_{i=2N+1}^{3N}\sum_{j=2M+1}^{3M}\left[\sum_{S=1}^{2}\sum_{k=1}^{N}\sum_{\ell=1}^{M} a_{k,\ell}^{S} G_\kappa(X_{i-2N,j-2M}^2,\xi_S^{k,\ell})\right. \\
&\left.-\sum_{k=1}^{N}\sum_{\ell=1}^{M} b_{k,\ell} G_\kappa(X_{i-2N,j-2M}^2,\xi_3^{k,\ell}) - u_2^p(X_{i-2N,j-2M}^2)\right]^2 \\
&+\sum_{i=3N+1}^{4N}\sum_{j=3M+1}^{4M}\left[\sum_{S=1}^{2}\sum_{k=1}^{N}\sum_{\ell=1}^{M} a_{k,\ell}^{S} \frac{\partial G_\kappa}{\partial n}(X_{i-3N,j-3M}^2,\xi_S^{k,\ell})\right. \\
&\left.-\sum_{k=1}^{N}\sum_{\ell=1}^{M} b_{k,\ell} \frac{\partial G_\kappa}{\partial n}(X_{i-3N,j-3M}^2,\xi_3^{k,\ell}) - \frac{\partial u_2^p}{\partial n}(X_{i-3N,j-3M}^2)\right]^2 \\
&+\lambda_1\left\{\sum_{S=1}^{2}\sum_{k=1}^{N}\sum_{\ell=1}^{M}\left(a_{k,\ell}^{S}\right)^2 + \sum_{k=1}^{N}\sum_{\ell=1}^{M} b_{k,\ell}^2\right\} \\
&+\lambda_2\left\{\sum_{i=2}^{N}\sum_{j=1}^{M}\left(\frac{r_{i,j}-r_{i-1,j}}{2\pi/N}\right)^2 + \sum_{i=1}^{N}\sum_{j=2}^{M}\left(\frac{r_{i,j}-r_{i,j-1}}{\pi/M}\right)^2\right\}. \qquad (26)
\end{aligned}
$$

The above minimization imposes $4NM$ regularised equations in the $4NM$ unknowns $(\mathbf{a},\mathbf{b},\mathbf{r})$. The noisy flux data g^ϵ is input as

$$
g^\epsilon(X_{i,j}^1) = (1+\rho_{i,j}\ p)g(X_{i,j}^1), \quad i=\overline{1,N},\ j=\overline{1,M}, \qquad (27)
$$

where p represents the percentage of noise and $\rho_{i,j}$ is a pseudo-random noisy variable drawn from a uniform distribution in [–1, 1] using the MATLAB © command `-1+2*rand(1,NM)`. The noise in (27) is multiplicative but additive random noise drawn from a Gaussian normal distribution can be also be considered.

In equation (26), the normal derivative of G_κ, via (19), is given by

$$
\frac{\partial G_\kappa}{\partial n}(x,\xi) = \begin{cases} -\frac{(x-\xi)\cdot n}{|x-\xi|^3} & \text{if } \kappa = 0 \\ \frac{(-i\kappa|x-\xi|-1)\exp(-i\kappa|x-\xi|)}{|x-\xi|^3}(x-\xi)\cdot n & \text{if } i\kappa \in \mathbb{R}_-^* \\ \frac{(i\kappa|x-\xi|-1)\exp(i\kappa|x-\xi|)}{|x-\xi|^3}(x-\xi)\cdot n & \text{if } \kappa \in \mathbb{R}_+^* \end{cases} \qquad (28)
$$

Also, in the case of the Helmholtz equation when we will employ the non-singular version of G_κ given by (20) instead of (19) (for $\kappa \in \mathbb{R}_+^*$) we have

$$
\frac{\partial G_\kappa}{\partial n}(x,\xi) = \frac{(\kappa|x-\xi|\cos(\kappa|x-\xi|) - \sin(\kappa|x-\xi|))}{|x-\xi|^3}(x-\xi)\cdot n \quad \text{if } \kappa \in \mathbb{R}_+^*. \qquad (29)
$$

In (26), the normal n to the boundary $\partial\Omega_1$ is given by

$$n(X) = \begin{cases} \cos(\theta)\sin(\phi)\boldsymbol{i} + \sin(\theta)\sin(\phi)\boldsymbol{j} + \cos(\phi)\boldsymbol{k}, & X \in \partial\Omega, \\ \frac{-1}{\sqrt{(r^2+r_\phi^2)\sin^2(\phi)+r_\theta^2}}\Big[(-r_\theta\sin(\theta) + r_\phi\sin(\phi)\cos(\phi)\cos(\theta) - r\sin^2(\phi)\cos(\theta))\boldsymbol{i} \\ \quad +(r_\theta\cos(\theta) + r_\phi\sin(\phi)\cos(\phi)\sin(\theta) - r\sin^2(\phi)\sin(\theta))\boldsymbol{j} \\ \quad -\sin(\phi)(r_\phi\sin(\phi) + r\cos(\phi))\boldsymbol{k}\Big], & X \in \partial\Omega_2, \end{cases} \tag{30}$$

where $\boldsymbol{i} = (1,0,0)$, $\boldsymbol{j} = (0,1,0)$, $\boldsymbol{k} = (0,0,1)$, and the r_θ and r_ϕ denote the partial derivative with respect to θ and ϕ, respectively. In (30), the derivative r_θ and r_ϕ are approximated using backward finite differences as

$$r_\theta(\theta_i,\phi_j) \approx \frac{r_{i,j} - r_{i-1,j}}{2\pi/N} \qquad i = \overline{2,N},\ j = \overline{1,M}, \tag{31}$$

$$r_\phi(\theta_i,\phi_j) \approx \frac{r_{i,j} - r_{i,j-1}}{\pi/M} \qquad i = \overline{1,N},\ j = \overline{2,M}. \tag{32}$$

The minimization of the functional (24) is performed using the Matlab toolbox routine `lsqnonlin` which does not require the user to provide the gradient and, in addition, it offers the option of imposing lower and upper bounds on the elements of the vector of unknowns $(\mathbf{a},\mathbf{b},\mathbf{r})$ through the vectors `lb` and `ub`.

4 Numerical results and discussion

In all numerical experiments, the initial guess for the unknown vectors $\mathbf{a}$ and $\mathbf{b}$ are $\mathbf{0}$, and the initial guess for Ω_2 is a sphere centred at the origin of radius 0.7. The Matlab toolbox routine `lsqnonlin` was run iteratively until a user-specified tolerance of $XTOL = 10^{-6}$ was achieved, or until when a user-specified maximum number of iterations $MAXCAL = 1000 \times 4MN$ was reached. We have also set the simple bounds on the variable $(\mathbf{a},\mathbf{b},\mathbf{r})$ as the box $[-10^{10},10^{10}]^{2NM} \times [-10^{10},10^{10}]^{NM} \times (0,1)^{NM}$. The choices of the regularization parameters λ_1 and λ_2 in (26) were based on trial and error, and, in fact, we take for simplicity $\lambda_1 = \lambda_2 =: \lambda$, but nevertheless more research needs to be undertaken in the future on the rigorous selection of multiple regularization parameters, see e.g. [6].

In what follows, we take $\kappa = 0$ for Examples 1(a) and 2(a), $\kappa' = 1$ for Examples 1(b) and 2(b), and $\kappa = 1$ for Examples 1(c) and 2(c).

4.1 Reconstructing a spherical source domain

We consider retrieving a sphere centred at the origin of radius $R_0 = 0.5$. That is, we seek the star-shape approximation (21) for the spherical radius function

$$r(\theta,\phi) \equiv R_0 = 0.5, \quad \theta \in [0,2\pi),\ \phi \in [0,\pi). \tag{33}$$

For the three cases of κ that we consider we take the following examples with analytical solutions satisfying equations (5), (6) and (12).

4.1.1 Example 1(a). ($\kappa = 0$, Laplace's equation)

In the case $\kappa = 0$, equations (5), (6) and (12) become

$$\nabla^2 u_1 = 0 \quad \text{in } \Omega_1, \tag{34}$$
$$\nabla^2 u_2 = 1 \quad \text{in } \Omega_2, \tag{35}$$
$$\nabla^2 u_2^h = 0 \quad \text{in } \Omega_2. \tag{36}$$

From (14) we also have that

$$u_2^p(r,\theta,\phi) = \frac{r^2}{6}, \quad (r,\theta,\phi) \in \mathbb{R}_+ \times [0,2\pi) \times [0,\pi). \tag{37}$$

We then take the analytical solutions of the equations (34)-(36) to be given by

$$u_1(r,\theta,\phi) = \frac{R_0^2}{6} - \frac{R_0^3}{3r} \quad (r,\theta,\phi) \in (R_0,1) \times [0,2\pi) \times [0,\pi), \tag{38}$$
$$u_2(r,\theta) = \frac{r^2}{6} - \frac{R_0^2}{3}, \quad (r,\theta,\phi) \in (R_0,1) \times [0,2\pi) \times [0,\pi), \tag{39}$$
$$u_2^h(r,\theta,\phi) = -\frac{R_0^2}{3}, \quad (r,\theta,\phi) \in (R_0,1) \times [0,2\pi) \times [0,\pi). \tag{40}$$

Based on (38), the input Cauchy data (9) and (10) are given by

$$u_1(1,\theta,\phi) = f(\theta,\phi) = \frac{R_0^2}{6} - \frac{R_0^3}{3}, \quad \theta \in [0,2\pi),\ \phi \in [0,\pi), \tag{41}$$
$$\frac{\partial u_1}{\partial n}(1,\theta,\phi) = g(\theta,\phi) = \frac{R_0^3}{3}, \quad \theta \in [0,2\pi),\ \phi \in [0,\pi), \tag{42}$$

and, based on (21) and (37), the transmission interface conditions (15) and (16) become

$$u_1\Big(r(\theta,\phi),\theta,\phi\Big) = u_2^h(r(\theta,\phi),\theta,\phi) + \frac{r^2(\theta,\phi)}{6}, \quad \theta \in [0,2\pi),\ \phi \in [0,\pi), \tag{43}$$
$$\frac{\partial u_1}{\partial n}\Big(r(\theta,\phi),\theta,\phi\Big) = \frac{\partial u_2^h}{\partial n}(r(\theta,\phi),\theta,\phi) + \frac{r(\theta,\phi)}{3}, \quad \theta \in [0,2\pi),\ \phi \in [0,\pi). \tag{44}$$

From [9, 13], we know that (33), (38) and (39) is the unique solution of the problem (34), (35), (41), (42), (7) and (8) in the class of star-shaped domains (21) with respect to the origin. In order to find this solution, we solve numerically, as described in Section 3, the inverse problem given by equations (34), (37), (41)-(44) to retrieve the analytical solution $(r(\theta,\phi), u_1(r,\theta,\phi), u_2^h(r,\theta,\phi))$ given by equations (33), (38) and (40). Also, once u_2^h has been obtained, equations (11) and (37) yield u_2.

4.1.2 Example 1(b). ($\kappa = i\kappa'$ with $\kappa' \in \mathbb{R}_+^*$, modified Helmholtz equation)

In the case $\kappa = i\kappa'$ with $\kappa' \in \mathbb{R}_+^*$, equations (5), (6) and (12) become

$$\nabla^2 u_1 - \kappa'^2 u_1 = 0 \quad \text{in } \Omega_1, \tag{45}$$
$$\nabla^2 u_2 - \kappa'^2 u_2 = 1 \quad \text{in } \Omega_2, \tag{46}$$
$$\nabla^2 u_2^h - \kappa'^2 u_2^h = 0 \quad \text{in } \Omega_2. \tag{47}$$

From (14) we also have that

$$u_2^p(r,\theta,\phi) = -\frac{1}{\kappa'^2} + \frac{\sinh(\kappa' r)}{r}, \quad (r,\theta,\phi) \in \mathbb{R}_+ \times [0,2\pi) \times [0,\pi). \tag{48}$$

We then take the analytical solutions of the equations (45)-(47) to be given by

$$u_1(r,\theta,\phi) = \frac{Ae^{\kappa' r} + Be^{-\kappa' r}}{r}, \quad (r,\theta,\phi) \in (R_0,1) \times [0,2\pi) \times [0,\pi), \tag{49}$$

$$u_2(r,\theta,\phi) = -\frac{1}{\kappa'^2} + \frac{\sinh(\kappa' r)}{r}, \quad (r,\theta,\phi) \in (0,R_0) \times [0,2\pi) \times [0,\pi), \tag{50}$$

$$u_2^h(r,\theta,\phi) = 0, \quad (r,\theta,\phi) \in (0,R_0) \times [0,2\pi) \times [0,\pi), \tag{51}$$

where

$$\begin{aligned} A &= \frac{e^{-\kappa' R_0}}{2}\Big(-\frac{R_0}{\kappa'^2} + \sinh(\kappa' R_0) + \cosh(\kappa' R_0) - \frac{1}{\kappa'^3}\Big), \\ B &= \frac{e^{\kappa' R_0}}{2}\Big(-\frac{R_0}{\kappa'^2} + \sinh(\kappa' R_0) - \cosh(\kappa' R_0) + \frac{1}{\kappa'^3}\Big), \end{aligned} \tag{52}$$

Based on (49), the input Cauchy data (9) and (10) are given by

$$u_1(1,\theta,\phi) = f(\theta,\phi) = Ae^{\kappa'} + Be^{-\kappa'}, \quad \theta \in [0,2\pi),\ \phi \in [0,\pi), \tag{53}$$

$$\frac{\partial u_1}{\partial n}(1,\theta,\phi) = g(\theta,\phi) = A(\kappa'-1)e^{\kappa'} - B(\kappa'+1)e^{-\kappa'}, \quad \theta \in [0,2\pi),\ \phi \in [0,\pi), \tag{54}$$

and, based on (21) and (48), the transmission interface conditions (15) and (16) become

$$u_1(r(\theta,\phi),\theta,\phi) = u_2^h(r(\theta,\phi),\theta,\phi) + \frac{\sinh(\kappa' r)}{r} - \frac{1}{\kappa'^2}, \quad \theta \in [0,2\pi),\ \phi \in [0,\pi), \tag{55}$$

$$\frac{\partial u_1}{\partial n}(r(\theta,\phi),\theta,\phi) = \frac{\partial u_2^h}{\partial n}(r(\theta,\phi),\theta,\phi) + \frac{\kappa' r\cosh(\kappa' r) - \sinh(\kappa' r)}{r^2},\ \theta \in [0,2\pi),\ \phi \in [0,\pi). \tag{56}$$

Then, we solve numerically, as described in Section 3, the inverse problem given by equations (45), (47), (53)-(56) to retrieve the analytical solution $(r(\theta,\phi), u_1(r,\theta,\phi), u_2^h(r,\theta,\phi))$ given by equations (33), (49) and (51). Also, once u_2^h has been obtained, equations (11) and (48) yield u_2.

4.1.3 Example 1(c). ($\kappa \in \mathbb{R}_+^*$, Helmholtz equation)

In the case $i\kappa$ with $\kappa \in \mathbb{R}_+^*$, we take the analytical solutions of equations (5), (6) and (11) to be given by

$$u_1(r,\theta,\phi) = \frac{A\cos(\kappa r) + B\sin(\kappa r)}{r}, \quad (r,\theta,\phi) \in (R_0,1) \times [0,2\pi) \times [0,\pi), \tag{57}$$

$$u_2(r,\theta,\phi) = \frac{1}{\kappa^2} + \frac{\sin(\kappa r)}{r}, \quad (r,\theta,\phi) \in (0,R_0) \times [0,2\pi) \times [0,\pi), \tag{58}$$

$$u_2^h(r,\theta,\phi) = 0, \quad (r,\theta,\phi) \in (0,R_0) \times [0,2\pi) \times [0,\pi), \tag{59}$$

where

$$A = \frac{1}{\kappa^2}\Big(\cos(\kappa R_0) - \frac{\sin(\kappa R_0)}{\kappa R_0}\Big), \quad B = 1 + \frac{1}{\kappa^2}\Big(\sin(\kappa R_0) + \frac{\cos(\kappa R_0)}{\kappa R_0}\Big). \tag{60}$$

From (14) we also have that

$$u_2^p(r,\theta,\phi) = \frac{1}{\kappa^2} + \frac{\sin(\kappa r)}{r}, \quad (r,\theta,\phi) \in \mathbb{R}_+ \times [0,2\pi) \times [0,\pi). \tag{61}$$

Based on (57), the input Cauchy data (9) and (10) are given by

$$u_1(1,\theta,\phi) = f(\theta,\phi) = A\cos(\kappa) + B\sin(\kappa), \quad \theta \in [0,2\pi),\ \phi \in [0,\pi), \tag{62}$$

$$\frac{\partial u_1}{\partial n}(1,\theta,\phi) = g(\theta,\phi) = -A(\kappa\sin(\kappa) + \cos(\kappa)) + B(\kappa\cos(\kappa) - \sin(\kappa)),$$
$$\theta \in [0,2\pi),\ \phi \in [0,\pi), \tag{63}$$

and, based on (21) and (61), the transmission interface conditions (15) and (16) become

$$u_1(r(\theta,\phi),\theta,\phi) = u_2^h(r(\theta,\phi),\theta,\phi) + \frac{1}{\kappa^2} + \frac{\sin(\kappa r)}{r}, \quad \theta \in [0,2\pi),\ \phi \in [0,\pi), \tag{64}$$

$$\frac{\partial u_1}{\partial n}(r(\theta,\phi),\theta,\phi) = \frac{\partial u_2^h}{\partial n}(r(\theta,\phi),\theta,\phi) + \frac{\kappa r\cos(\kappa r) - \sin(\kappa r)}{r^2}, \quad \theta \in [0,2\pi),\ \phi \in [0,\pi). \tag{65}$$

Then, we solve numerically, as described in Section 3, the inverse problem given by equations (5), (12), (62)-(66) to retrieve the analytical solution $(r(\theta), u_1(r,\theta), u_2^h(r,\theta))$ given by equations (33), (57) and (59). Also, once u_2^h has been obtained, equations (11) and (61) yield u_2.

Initially, we have performed several numerical runs with various values of the input MFS parameters and, for illustrative purposes, we have decided to show results only for a typical selected set of results obtained with $\delta = 0.5$, $R = 2$ and $N = M = 10$.

We consider first the case of exact data, i.e. $p = 0$ in equation (27). Figure 1 shows the unregularised nonlinear least-squares objective function (26) with $\lambda_1 = \lambda_2 = 0$, as a function of the number of iterations for Examples 1(a)–1(c). From this figure it can be seen that a monotonic decreasing convergence is obtained for all examples.

In Figure 2, we present the numerically reconstructed sphere for various numbers of iterations for no noise and no regularization as well as the correct sphere to be reconstructed for Example 1(a). From this figure, it can be seen that even if the input data is exact, as the number of iterations increases the numerical solution becomes more inaccurate. This is to be expected because no regularization has been imposed yet and the inverse problem under investigation is ill-posed. Consequently, in order to restore stability regularization should be employed with a positive regularization parameter $\lambda = \lambda_1 = \lambda_2$ in (26).

Figures 3 and 4 show the higher accuracy and stabilising effect that the regularization has on the retrieved shapes for values of λ between 10^{-3} and 10^{-1}.

We also perturb by a large amount of $p = 10\%$ noise the flux g, as in equation (27), in order to investigate further the stability of the numerical solution. The root mean square errors (RMSE)

$$\text{RMSE} = \sqrt{\frac{1}{MN}\sum_{i=1}^{N}\sum_{j=1}^{M}(r_{i,j} - 0.5)^2} \tag{66}$$

obtained with various values of the regularization parameter $\lambda = \lambda_1 = \lambda_2$ after 200 iterations for Examples 1(a)-1(c) are given in Table 1. From this table, we observe that overall λ values between 10^{-3} and 10^{-2} yield the most accurate and stable results for the reconstruction of the spherical source domain (33). We also mention that elsewhere in [9] we have retrieved an ellipsoid, in another application of the MFS for shape identification in electrical resistance tomography.

4.2 Reconstructing an acorn source domain

We consider now reconstructing a more complicated shape of a source domain Ω_2 having an acorn shape, [22], described parametrically by

$$r(\theta,\phi)=0.2\Big(0.6+\sqrt{4.25+2\cos(3\phi)}\Big),\quad \theta\in[0,2\pi),\ \phi\in[0,\pi). \tag{67}$$

In addition to being of a more irregular shape than the previous simple spherical domain (33), it also prevents analytical solutions for u being explicity available. In this case, the flux Neumann data (10) is simulated numerically by solving the direct well-posed problem given by equations (5)-(9) with the Dirichlet data in (9) given by

$$u_1(1,\theta,\phi)=f(\theta,\phi)=0,\quad (\theta,\phi)\in[0,2\pi)\times[0,\pi), \tag{68}$$

when the source domain Ω_2 is known and its boundary $\partial\Omega_2$ given by (21) and (67). Using the decomposition (11) we, in fact, solve (5), (12), (15), (16) and (68) using the MFS expansions (17) and (18) to determine the solutions u_1 and u_2^h. This recasts into solving the following linear system of $3MN$ equations with $3MN$ unknowns $\mathbf{a}=(a_{i,j}^S)_{i=\overline{1,N},j=\overline{1,M},S=1,2}$ and $\mathbf{b}=(b_{i,j})_{i=\overline{1,N},j=\overline{1,M}}$:

$$\sum_{S=1}^{2}\sum_{i=1}^{N}\sum_{j=1}^{M}a_{i,j}^S G_\kappa(X_{k,\ell}^1,\xi_S^{i,j})=0,\quad k=\overline{1,N},\ell=\overline{1,M}, \tag{69}$$

$$\sum_{S=1}^{2}\sum_{i=1}^{N}\sum_{j=1}^{M}a_{i,j}^S G_\kappa(X_{k,\ell}^2,\xi_S^{i,j})-\sum_{i=1}^{N}\sum_{j=1}^{M}b_{i,j}G_\kappa(X_{k,\ell}^2,\xi_3^{i,j})=u_2^p(X_{k,\ell}^2),\quad k=\overline{1,N},\ell=\overline{1,M}, \tag{70}$$

$$\sum_{S=1}^{2}\sum_{i=1}^{N}\sum_{j=1}^{M}a_{i,j}^S \frac{\partial G_\kappa}{\partial n}(X_{k,\ell}^2,\xi_S^{i,j})-\sum_{i=1}^{N}\sum_{j=1}^{M}b_{i,j}\frac{\partial G_\kappa}{\partial n}(X_{k,\ell}^2,\xi_3^{i,j})=\frac{\partial u_2^p}{\partial n}(X_{k,\ell}^2),\quad k=\overline{1,N},\ell=\overline{1,M}. \tag{71}$$

In (30), when the direct problem is solved we need to input, from (67), that $r_\theta=0$ and $r_\phi=-\frac{0.6\sin(3\phi)}{\sqrt{4.25+2\cos(3\phi)}}$. Otherwise, in the inverse problem we need to use the finite-difference approximations (31) and (32). In (70), the expression for u_2^p is given by (13) or (14), whilst in (71) the expression for the normal derivative is given by

$$\frac{\partial u_2^p}{\partial n}=\nabla u_2^p\cdot n,$$

where n is given by (30).

The numerical flux $g(\theta,\phi)$, calculated by differentiating equation (17), is plotted, as a function $\theta\in[0,2\pi),\ \phi\in[0,\pi)$ in Figures 5–7 for $\kappa=0$ (Example 2(a)), $\kappa'=1$ (Example 2(b)) and $\kappa=1$ (Example 2(c)), respectively, obtained with $\delta=0.3, R=1.5$ and various $M=N\in\{10,20,40\}$. From these figures it can be seen that the numerical results are convergent, as the number of degrees of freedom increases. Ten evenly spread points out of the curves $N=M=20$ further perturbed by $p=10\%$ noise are chosen as the Neumann

numerically simulated flux data (10) in the inverse problem which is solved using $\delta = 0.3$, $R = 1.5$ and $N = M = 10$. The numerically obtained results with various values of the regularization parameter $\lambda = \lambda_1 = \lambda_2$ after 200 iterations are shown in Figures 8–10 for Examples 2(a)-2(c), respectively. From these figures it can be seen that $\lambda = 10^{-2}$ yields the most accurate and stable results for reconstruction of the acorn source domain (67).

5 Conclusions

In this paper, an inverse geometric problem which consists of reconstructing the unknown support of a volumetric source in three-dimensional elliptic equations from a single pair of exterior boundary Cauchy data has been investigated. The interesting generalization to the case of partial Cauchy data is deferred to a future work. The numerical method was based on the MFS combined with the minimization of the nonlinear regularized least-squares functional which was performed using the Matlab toolbox routine `lsqnonlin`. Several examples have been investigated showing that the numerical results are satisfactory reconstructions for the unknown support of a source domain with reasonable stability against inverting noisy data. In this paper, the choice of regularization parameter λ was based on trial and error by inspecting the results obtained by increasing $\lambda = 0$ (unregularized and unstable reconstructions) to larger values until stable and accurate results are obtained. The L-curve method could also be employed, as described in [18] for a different inverse geometric problem, but more research needs to be performed for the rigorous choice of the regularization parameter in the nonlinear Tikhonov regularization method.

Acknowledgements
B. Bin-Mohsin extends his appreciation to the Deanship of Scientific Research at King Saud University for funding this work through research group no RG-1437-019. The comments and suggestions made by the referees are gratefully acknowledged.

References

1. C.J.S. Alves and C.S. Chen (2005) A new method of fundamental solutions applied to nonhomogeneous elliptic problems, *Advances in Computational Mathematics* **23**, 125-142.

2. B. Bin-Mohsin and D. Lesnic (2012) Determination of inner boundaries in modified Helmholtz inverse geometric problems using the method of fundamental solutions, *Mathematics and Computers in Simulation* **82**, 1445-1458.

3. B. Bin-Mohsin and D. Lesnic (2017) Reconstruction of a source domain from boundary measurements, *Applied Mathematical Modelling*, **45**, 925-939.

4. A. Canelas, A. Laurain and A.A. Novotny (2014) A new reconstruction method for the inverse potential problem, *Journal of Computational Physics* **268**, 417-431.

5. W. Chen and Y.C. Hon (2003) Numerical investigation on convergence of boundary knot method in the analysis of homogeneous Helmholtz, modified Helmholtz, and convection-

diffusion problems, *Computer Methods in Applied Mechanics and Engineering* **192**, 1859-1875.

6. Z. Chen, Y. Lu, Y. Xu and H. Yang (2008) Multi-parameter Tikhonov regularization for linear ill-posed operator equations, *Journal of Computational Mathematics* **26**, 37-55.

7. T.E. Dyhoum, R.G. Aykroyd and D. Lesnic (2017) Solving the inverse three-dimensional continuous model of electrical resistance tomography using the method of fundamental solutions and the Markov chain Monte Carlo approach, In: *Proceedings of the Eleventh UK Conference on Boundary Integral Methods (UKBIM11)*, (ed. D. Chappell), Nottingham Trent University: Publications, Chapter 6, pp.43-52.

8. M.A. Golberg (1994) The method of fundamental solutions for Poisson's equation, In: *Boundary Element Technology IX, BETECH94*, (eds. C.A. Brebbia and A.J. Kassab), Computational Mechanics Publications, Southampton, pp.299-307.

9. F. Hettlich and W. Rundell (1996) Iterative methods for the reconstruction of an inverse potential problem, *Inverse Problems* **12**, 251-266.

10. M. Ikehata (1999) Reconstruction of a source domain from the Cauchy data, *Inverse Problems* **15**, 637-643.

11. V. Isakov (1990) *Inverse Source Problems*, Mathematical Surveys and Monographs, Vol.**34**, Providence, RI, American Mathematical Society.

12. V. Isakov (2006) *Inverse Problems for Partial Differential Equations*, 2nd edn., Springer, New York.

13. V. Isakov, S. Leung and J. Qian (2011) A fast local level set method for inverse gravimetry, *Communications in Computational Physics* **10**, 1044-1070.

14. K. Ito and J.-C. Liu (2013) Recovery of inclusions in 2D and 3D domains for Poisson's equation, *Inverse Problems* **29**, 075005 (19 pages).

15. B. Jin and Y. Zheng (2005) Boundary knot method for some inverse problems associated with the Helmholtz equation, *International Journal for Numerical Methods in Engineering* **62**, 1636-1651.

16. B. Jin and W. Chen (2006) Boundary knot method based on geodesic distance for anisotropic problems, *Journal of Computational Physics* **215**, 614-629.

17. A. Karageorghis, D. Lesnic and L. Marin (2011) The MFS for inverse geometric problems, *Inverse Problems and Computational Mechanics*, Vol.**1**, (eds. L. Marin, L. Munteanu and V. Chiroiu), Editura Academiei, Bucharest, Romania, Chapter **8**, pp.191-216.

18. A. Karageorghis, D. Lesnic and L. Marin (2013) A moving pseudo-boundary MFS for three-dimensional void detection, *Advances in Applied Mathematics and Mechanics* **5**, 510-527.

19. D. Lesnic and B. Bin-Mohsin (2012) Inverse shape and surface heat transfer coefficient identification, *Journal of Computational and Applied Mathematics* **236**, 1876-1891.

20. R.G.S. Mamud, N.C. Roberty and C.J.S. Alves (2014) Analytical observability of symmetric star shaped sources for modified Helmholtz model, *8th International Conference on Inverse Problems in Engineering*, May 12-15, 2014, Poland, (eds. I. Szczygiel, A.J. Nowak and M. Rojczyk), pp.179-188.

21. W. Ring (1995) Identification of a core from boundary data, *SIAM Journal on Applied Mathematics*, **55**, 677-706.

22. P. Serranho (2007) A hybrid method for inverse scattering for sound-soft obstacles in $\mathbb{R}^3$, *Inverse Problems and Imaging*, **1**, 691-712.

Table 1: The RMSE (66) for the radial function $r(\theta, \phi)$, for $p = 10\%$ noise after 200 iterations, for Examples 1(a)-1(c).

λ	Example 1(a)	Example 1(b)	Example 1(c)
0	0.0634	0.1154	0.1934
10^{-4}	0.0791	0.1118	0.1854
10^{-3}	0.0303	0.0356	0.0754
10^{-2}	0.0186	0.0197	0.0597

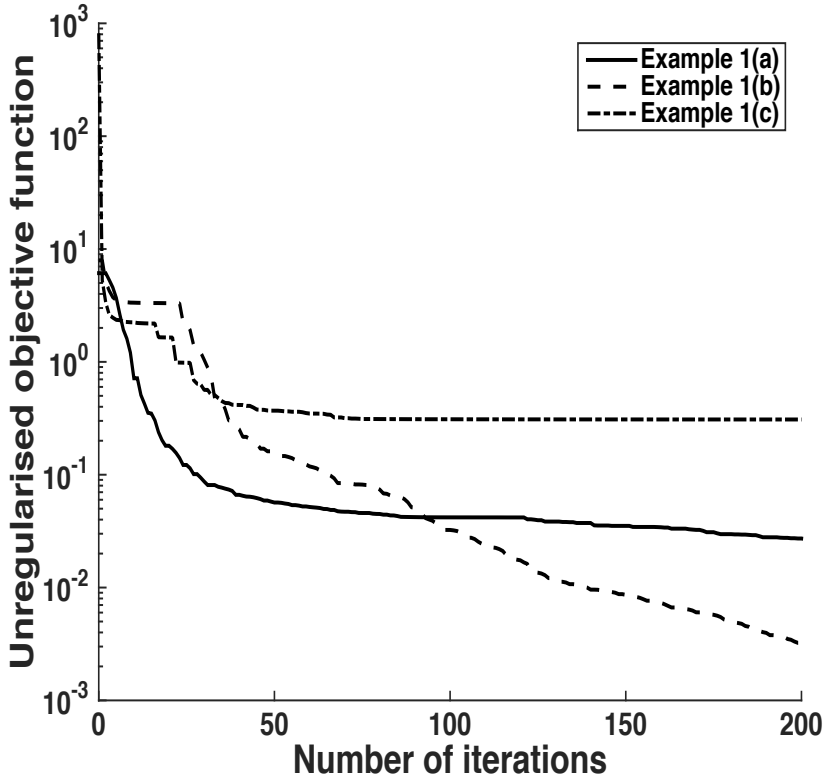

Figure 1: The unregularised objective function, as a function of the number of iterations, for no noise for Examples 1(a)–1(c).

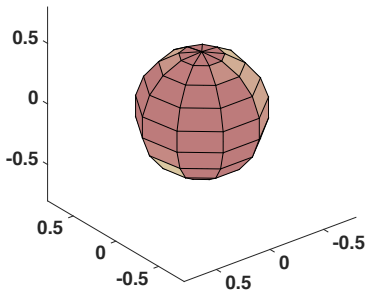

(a) Exact

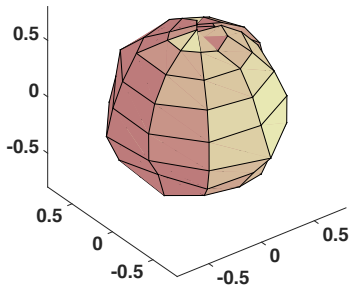

(b) iter=10

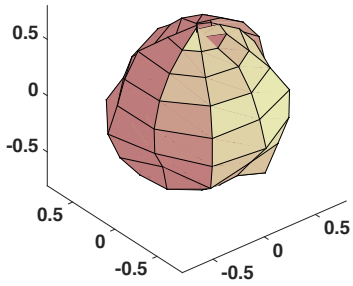

(c) iter=100

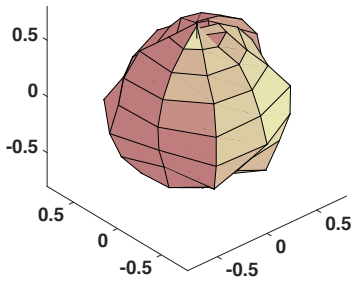

(d) iter=200

Figure 2: The reconstructed volumetric source domain for various numbers of iterations for no noise and no regularization, for Example 1(a).

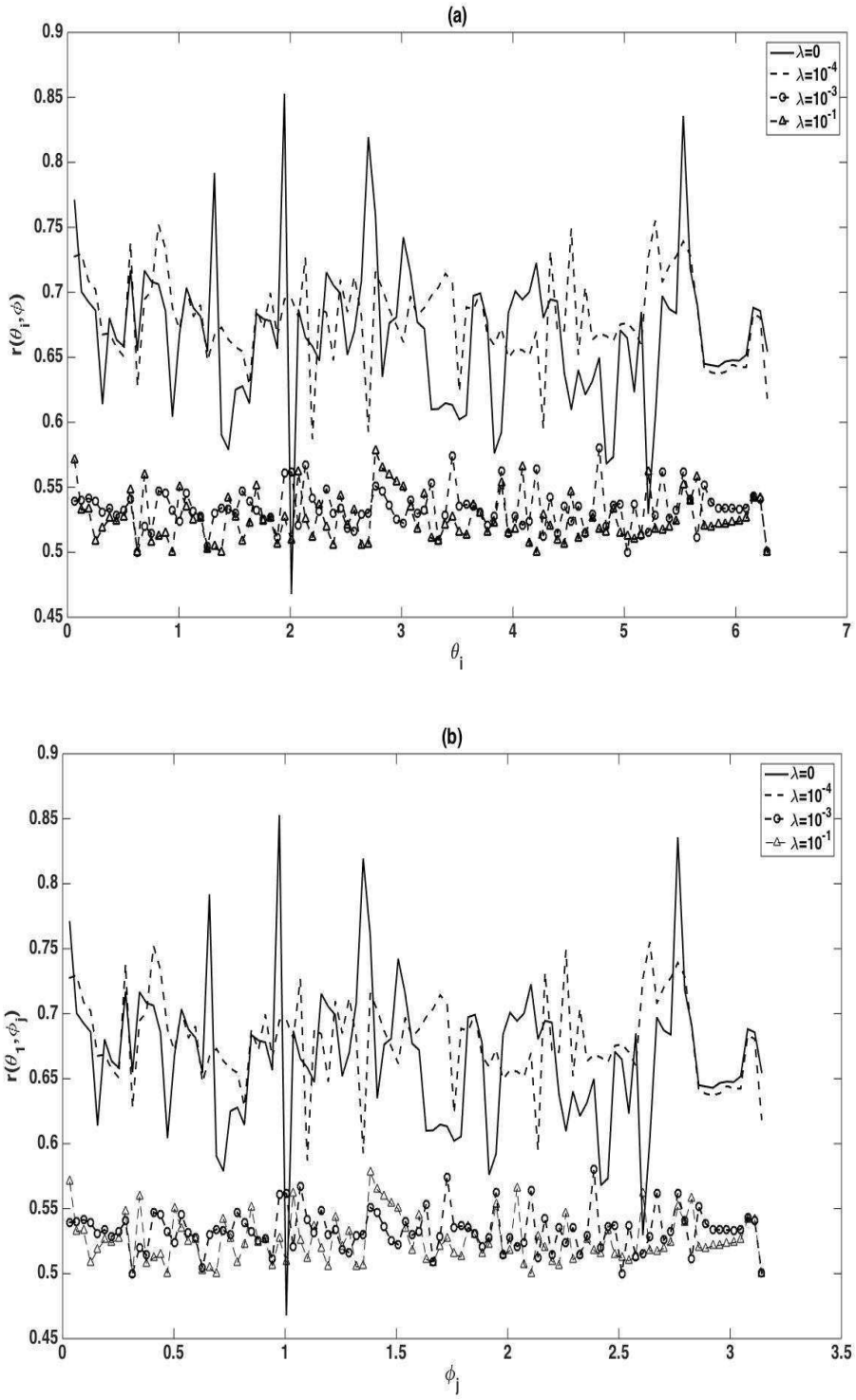

Figure 3: The retrieved radius (a) $r(\theta_i, \phi_1)$ for $i = \overline{1, N}$ and (b) $r(\theta_1, \phi_j)$ for $j = \overline{1, M}$, after 200 iterations for various $\lambda \in \{0, 10^{-4}, 10^{-3}, 10^{-1}\}$, no noise, for Example 1(a).

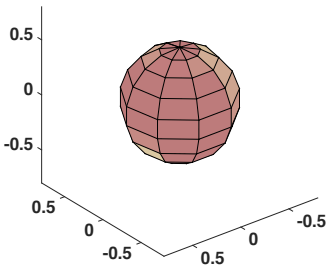

(a) Exact

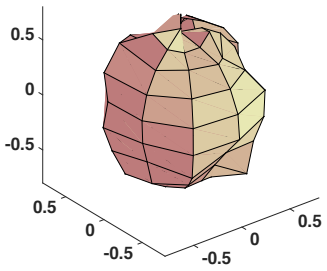

(b) $\lambda = 0$

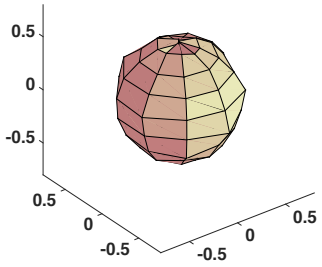

(c) $\lambda = 10^{-3}$

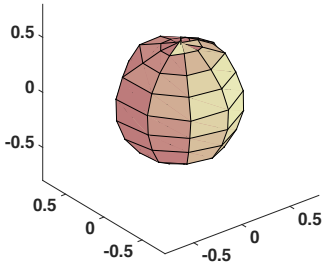

(d) $\lambda = 10^{-1}$

Figure 4: The reconstructed volumetric source domain after 200 iterations for no noise and regularization, for Example 1(a).

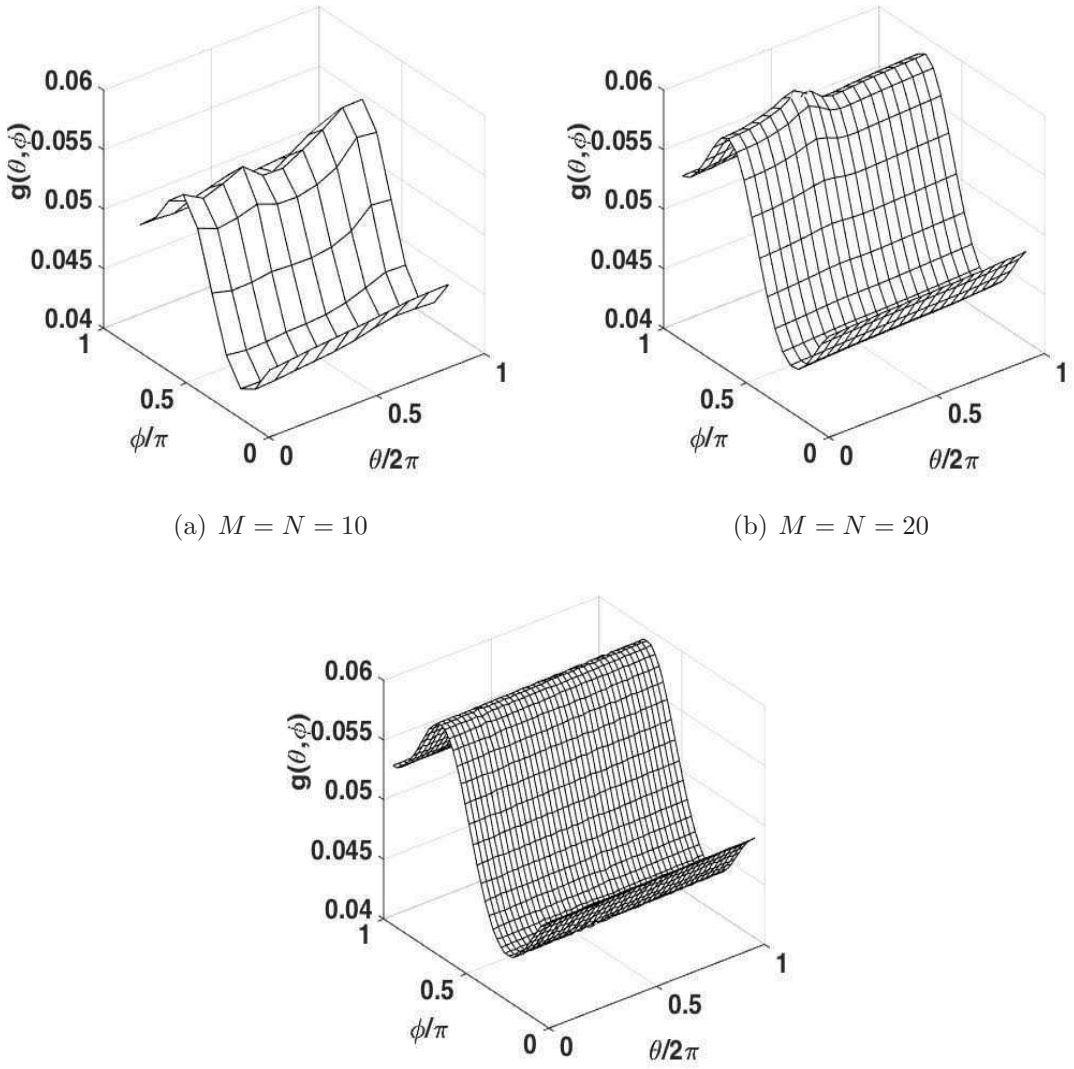

(a) $M = N = 10$

(b) $M = N = 20$

(c) $M = N = 40$

Figure 5: The normal derivative (10) obtained by solving the direct problem (5), (12), (15), (16) and (68) using the MFS with various values of $M = N \in \{10, 20, 40\}$ for $\kappa = 0$, Example 2(a).

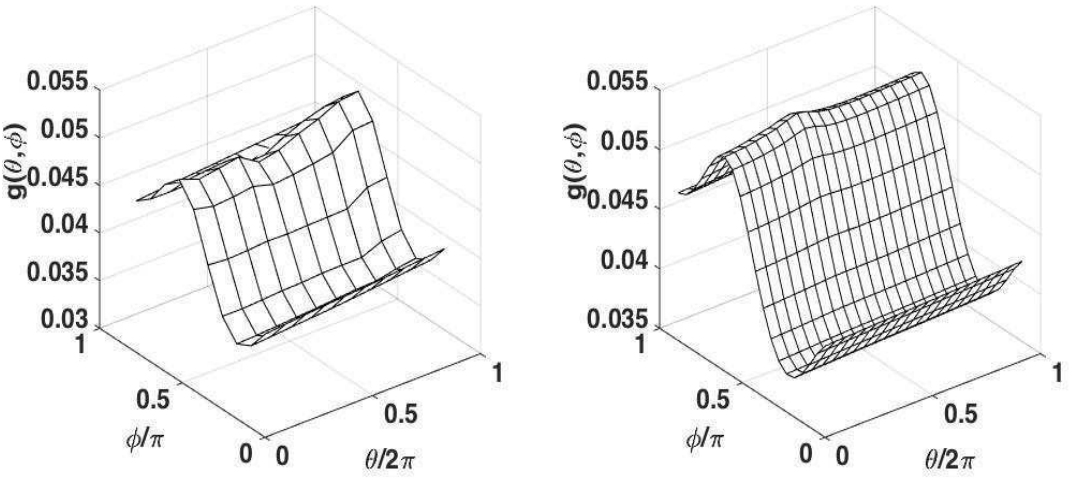

(a) $M = N = 10$

(b) $M = N = 20$

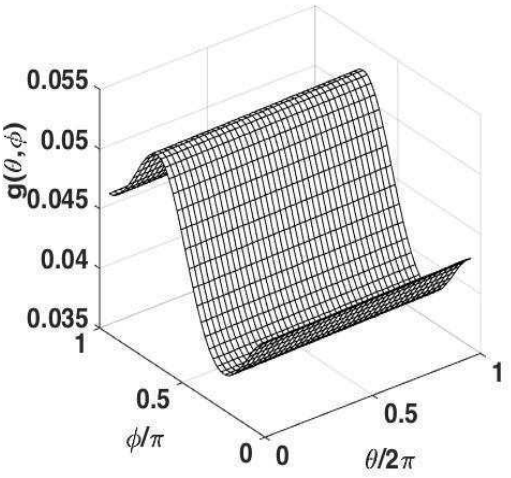

(c) $M = N = 40$

Figure 6: The normal derivative (10) obtained by solving the direct problem (5), (12), (15), (16) and (68) using the MFS with various values of $M = N \in \{10, 20, 40\}$ for $\kappa' = 1$, Example 2(b).

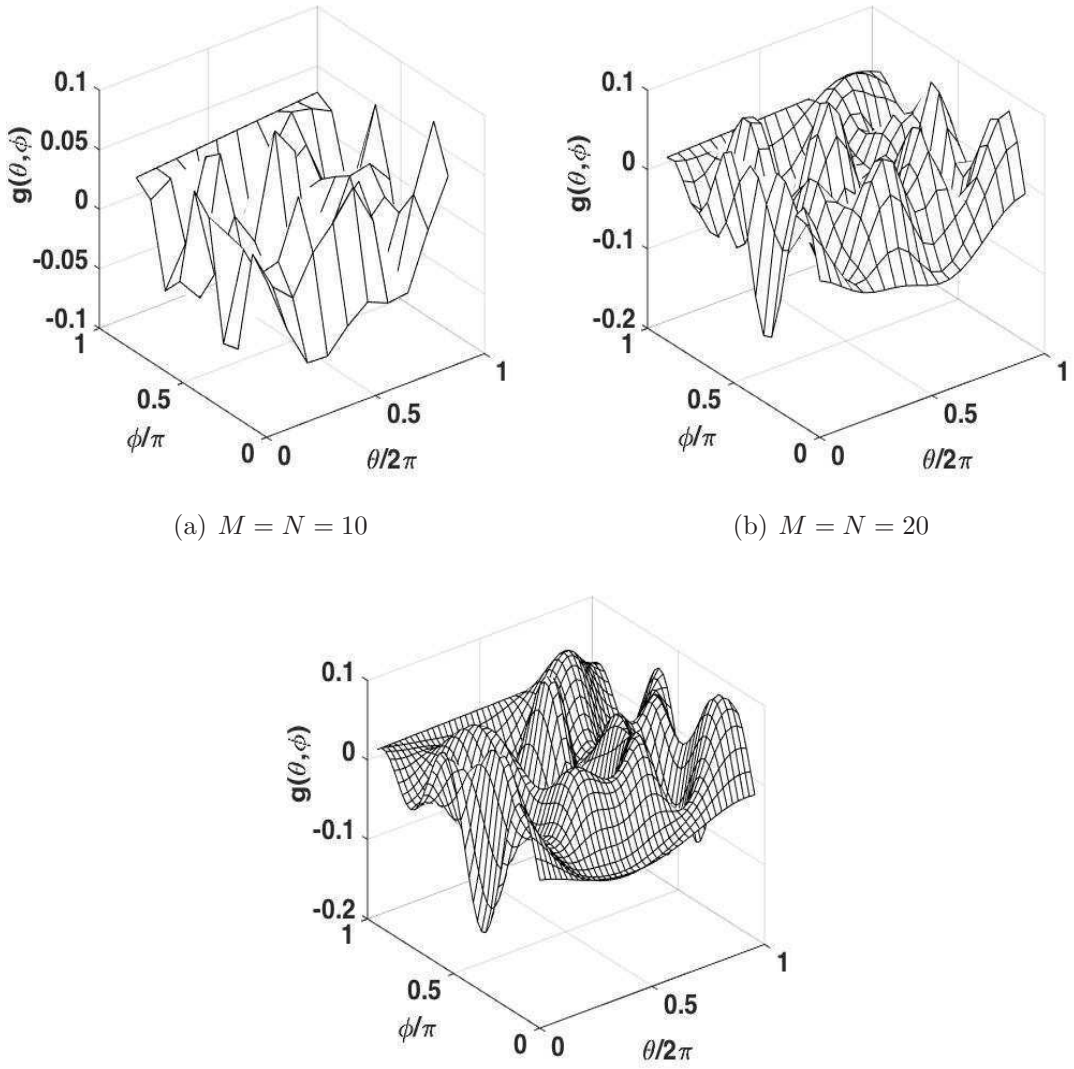

(a) $M = N = 10$

(b) $M = N = 20$

(c) $M = N = 40$

Figure 7: The normal derivative (10) obtained by solving the direct problem (5), (12), (15), (16) and (68) using the MFS with various values of $M = N \in \{10, 20, 40\}$ for $\kappa = 1$, Example 2(c).

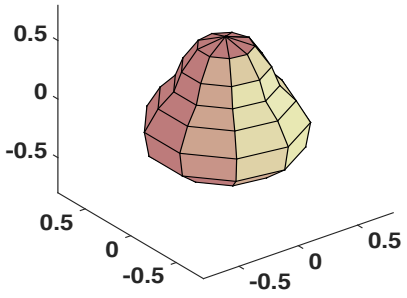

(a) Exact

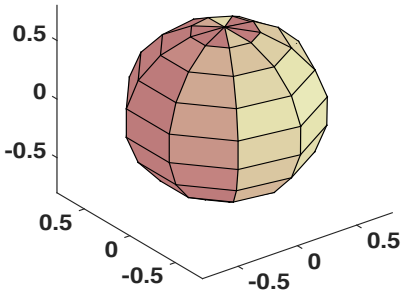

(b) $\lambda = 0$

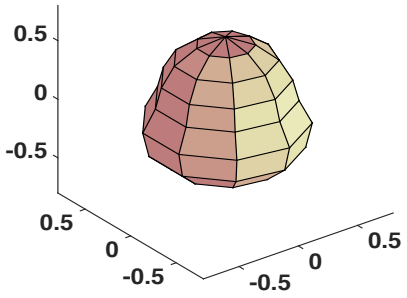

(c) $\lambda = 10^{-4}$

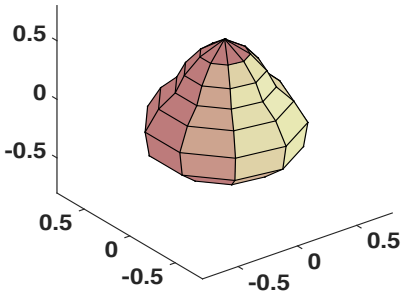

(d) $\lambda = 10^{-2}$

Figure 8: The reconstructed volumetric source domain after 200 iterations for $p = 10\%$ noise and regularization, for Example 2(a).

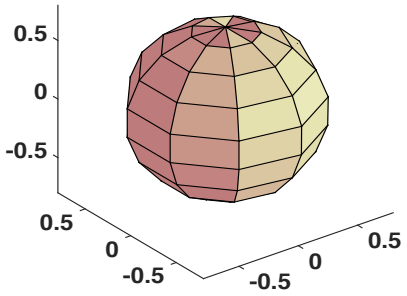

(a) $\lambda = 0$

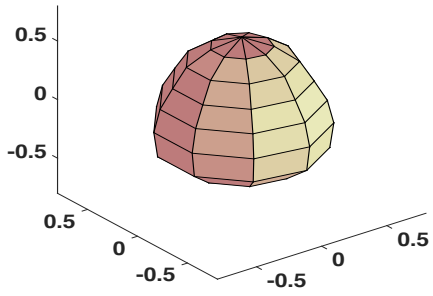

(b) $\lambda = 10^{-6}$

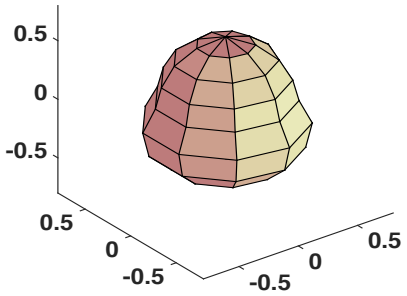

(c) $\lambda = 10^{-4}$

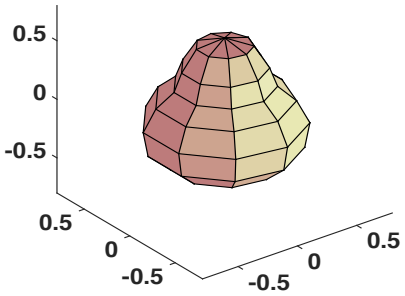

(d) $\lambda = 10^{-2}$

Figure 9: The reconstructed volumetric source domain after 200 iterations for $p = 10\%$ noise and regularization, for Example 2(b).

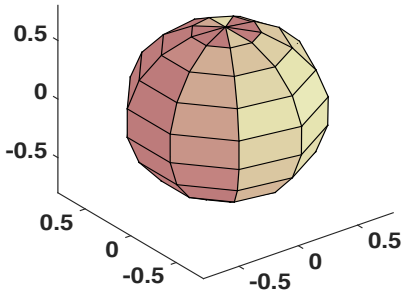

(a) $\lambda = 0$

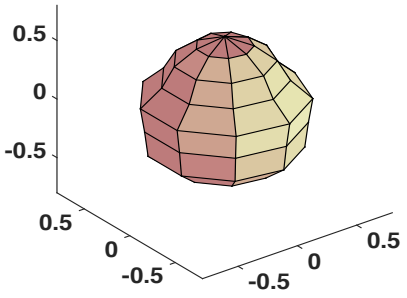

(b) $\lambda = 10^{-7}$

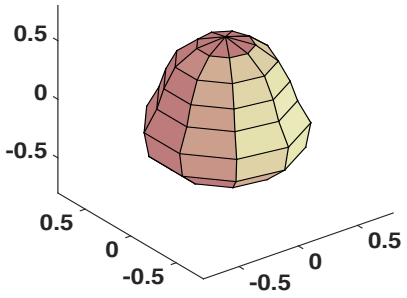

(c) $\lambda = 10^{-4}$

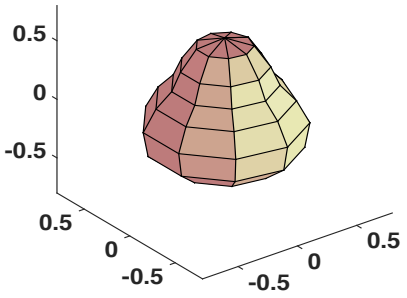

(d) $\lambda = 10^{-2}$

Figure 10: The reconstructed volumetric source domain after 200 iterations for $p = 10\%$ noise and regularization, for Example 2(c).